Astron. Astrophys. 325, 769–781 (1997)

ASTRONOMY
AND
ASTROPHYSICS

Molecular gas in the barred spiral M 100

I. The IRAM 30m map

M.J. Sempere and S. García-Burillo

Observatorio Astronómico Nacional, Campus Universitario, Apartado 1143, E-28800 Alcalá de Henares (Madrid), Spain
(sempere@oan.es, burillo@oan.es)

Received 30 January 1997 / Accepted 10 March 1997

Abstract. We present a study on the distribution, kinematics and evolution of the molecular gas disk in the barred SBbc spiral M100(NGC4321). The J=2–1 and J=1–0 lines of ^{12}CO have been mapped with the IRAM 30m telescope, with resolutions HPBW=12″ and HPBW=21″, within the inner 8kpc of the disk (1″=82pc, assuming D_{M100}=17.1Mpc). Complementary ^{13}CO(1–0) observations of the nucleus, spiral and interarm regions are used to study the nature of H_2 gas.

CO emission traces a markedly asymmetric two spiral-arm structure stretching out from a molecular gas bar. The CO bar has a diameter D∼90″ and it is aligned with the stellar bar seen in I and K band images (PA=110°). Arm I (II) springs off the western (eastern) side of the bar at r∼50″. Arm II is split up in two armlets (at r∼40-50″), it disappears and finally shows up at a position angle close to the major axis northern crossing (PA=330°). The splitting starts near the inner 3::1 resonance identified by Elmegreen et al (1992) in the enhanced optical images of M100. Molecular gas in the bar is strongly concentrated in a nuclear disk of r_{nucl} ∼30″ and $M(H_2)_{nucl}$=2.8 $10^9 M_\odot$.

Arms I-II display different arm-interarm contrasts (on average, $R_{a/ia}$(CO) increases with radius from 2.5 (r∼30″) up to 6.5 (r∼110″), being higher for arm I than for arm II. Also arms I-II relate differently to other spiral arm tracers, underlying the asymmetry in the disk. Comparison between CO, H I and H_α maps show that there is no *coherent* sequence in the relative location of the star formation tracers along the spiral arms. Evidences of triggering of star formation along spiral arms are poor: $R_{a/ia}(H_\alpha)$ is only ∼ 2 $R_{a/ia}$(CO) and systematic offsets between H_α and CO ridges (expected to lie downstream and upstream the spiral potential minimum, respectively, assuming trailing arms inside corotation) are hard to find and at places they are absent or even inverted.

CO reveals as the best tracer of gas kinematics in the inner disk. The CO rotation curve (V_{rot}) is steeper than the curves derived from the H I and H_α data. V_{rot} reaches 200km s^{-1} in less than 1kpc. The signature of the m=3 instability has been also identified in the CO derived velocity field. The magnitude and the sign of streaming motions, associated with the spiral arms and the bar, are consistent with the CO disk to be inside corotation (r_{cor}=110″). A secondary wave compression develops in the eastern side where arm II is split.

Massive star formation (MSF) is inhibited along the gaseous bar, indicating that M100 is an *evolved* barred system (Friedli and Benz, 1995). Star formation rate (measured as the ratio SFR=$F(H_\alpha)/I_{CO}$) is lower for the nuclear disk than for the disk itself. However we suspect the measurement of SFR to be subjected to major uncertainties: the $X=N(H_2)/I_{CO}$ conversion factor might be 3 times lower than implicitly assumed and to vary within the disk (lower for the interarm than for the arms and nuclear region) . Moreover extinction affects $F(H_\alpha)$ mostly in the nucleus where the classical Schmidt law breaks down paradoxically (SFR_{ND} ∼N^α_{gas}, α ∼1). MSF is set on at a distance r_c ∼ 12kpc where $N(H_2)$ approaches the Toomre (1964) gravitational instability threshold (N_c ∼7$M_\odot$). Also for r<r_c, the neutral gas is mostly in the H_2 phase. H I is underabundant in the inner 6kpc and cannot be accounted for by photodissociation of H_2 by H II regions.

Asymmetry in the observed molecular gas distribution and kinematics of M 100 seems related with the three-arm structure studied by Elmegreen and collaborators. Although the m=2 spiral mode is still predominant in M100, other secondary modes seem at interplay reflecting the secular evolution of the disk. Compared to M51, M100 appears as an *evolved* barred spiral.

Key words: galaxies: kinematics and dynamics of – galaxies: spiral – galaxies: individual – radio lines

1. Introduction

Predominance of molecular over atomic gas in many spirals makes CO emission lines to be the main tracer of neutral gas in the inner regions of spiral disks. The scarcity of complete studies on the distribution, kinematics, physical conditions and chemical abundances of molecular gas in spirals is understandable, in view of the instrumental limitations to overcome: the

Send offprint requests to: S. García-Burillo

requirements of high-resolution and sensitivity are fulfilled by few millimiter radiotelescopes. The completion of a good quality map on a nearby galaxy can be also time-consuming.

Still, the knowledge of the molecular gas response to density waves is essential to understand the mechanism of star formation in disks and its relation with spiral and barred structure. The complex and fragmented structure of neutral ISM invalidates partly the theoretical scenario envisaged to predict the evolution of gaseous disks. The response of the ensemble of molecular clouds might not even reach an equilibrium steady state (Casoli and Combes 1982, Combes and Gerin 1985, Roberts and Stewart 1987), blurring the picture of the classical time sequence across the spiral arms (molecular clouds form by shocked H I complexes at the entrance of the arms and give birth to massive stars, located downstream the spiral potential). The phase equilibrium between H I and H_2 might be more influenced by other factors as the z-gravitational potential. Indeed there is no satisfactory explanation for the observed radial distribution of H I and H_2 gas in spiral disks (Kennicut 1989). There is neither a clear understanding of the role of density waves in the SFR (Elmegreen and Elmegreen 1986, Elmegreen 1994)

The grand-design galaxy NGC4321(or M100) (classified as SABbc by de Vaucouleurs et al 1991) is an optimum candidate to test density wave theories predictions. Superposed to a well developed two-arm spiral structure seen in optical pictures there is a double bar pattern (a nuclear oval of r$\sim$15″ and a large stellar bar of r$\sim$60″, both visible in the I CCD image of Pierce(1986)) as well as a complex hierarchy of secondary features identified with a three arm mode (extending from the nucleus up to $\sim 0.9 R_{25}$, the presence of global patterns of spiral arm resonance phenomena (spurs at the 4:1 resonances) and a circle of star formation in the vicinity of corotation (Elmegreen et al 1992; hereafter called **E92**). The spectacular HST images of the center of this galaxy brought new elements to discuss the nature of the underlying mass distribution in the inner 1 kpc, still far to be understood.

M100 has the appropriate inclination (i=32°) and is nearby enough (D=17.1Mpc) to resolve its spiral+bar structure with the 30m beam. It is also a strong CO emitter (see García-Burillo et al 1994; hereafter called **GB94**). The ensemble of available observations on this galaxy at many wavelengths (optical, infrared, centimeter and millimeter lines and radio-continuum) bring precious information to be used in a multidisciplinary study. NGC4321, in contrast with M51, is apparently isolated, and therefore the present study offers the opportunity to compare in detail the properties of gaseous disks in a strongly interacting system and in an isolated spiral (and barred) galaxy.

We present here the first complete single-dish map of the M100 disk in the J=1-0 and J=2-1 rotational lines of ^{12}CO. **GB94** presented a map of the minor axis region in an attempt to identify the signature of the corotation resonance on the observed radial velocity field. Knapen et al 1996 (hereafter called **K96**) published a partial map made with the 45m Nobeyama antenna and covering certain segments of the spiral arms. In their survey there is hardly any point on the interarm region and the quality of the published observations is dubious. Neither the sensitivity nor the sampling of their data are sufficient and their conclusions are subject to major uncertainties. There are several aperture synthesis maps but they focus mainly on the nuclear region (Rand 1995, Sakamoto et al 1995). Rand and collaborators extended their survey to the southern spiral arm but they failed to detect the interarm gas: interferometers filter out the low spatial frequencies.

The data presented here possess high-resolution (21″in the 1-0 line and 12″in the 2-1 line) and sensitivity. They provide a direct measurement of the CO arm-interam contrast, the disk velocity field, the physical conditions of H_2 gas (we observed the 1-0 line of the main isotope ^{13}CO in different environments of the disk) and finally they allow a comparison with other spiral arm tracers (in particular H I and H_α) to analyze the star formation properties of the galaxy. The 30m data will be furtherly combined with a 2″resolution interferometer 40″field of the center. The combined data will be the observational basis of a model on the evolution of the molecular gas disk in this galaxy via numerical simulations of the clouds hydrodynamics (García-Burillo et al, in prep; hereafter referred as paper **II**).

The complete CO data set is presented in Sects. 2 and 3. Sect. 4 is devoted to compare molecular gas with other spiral arm tracers. Gas kinematics is the subject of Sect. 5. Physical conditions of the gas are analyzed in Sect. 6. Sects. 7 and 8 are devoted to discussions and conclusions of this work.

2. Observations

The observations were made from July to November 1995 with the IRAM 30 m telescope. Two SIS receivers, one operating in the 1.3 mm band (receiver temperature Tr(SSB)= 200-300 K, system temperature Tsys= 350-500K), and one in the 3 mm band (Tr(SSB)= 120-200 K; Tsys= 250-400 K) allowed simultaneous observations of the ^{12}CO J= 2-1 and 1-0 lines in July 1995. The winter period was devoted to observe the ^{12}CO J= 2-1 line and the J= 1-0 isotopic line of ^{13}CO.

Considerable effort was devoted to insure that data were of good quality. Most of the observations at 1.3 mm were made in winter, when the atmospheric opacity at 230GHz was less than 0.3. Low quality data taken during the July period at 1.3mm were finally discarded.

Observations were restricted to elevations >25 deg. In order to take advantage of the telescope high tracking accuracy (0.5″ r.m.s.) sub-maps were quickly scanned lasting 1-2 hour each, and followed systematically by pointing sessions on the nearby quasar 3C273 together with a calibration session on several reference positions near the center of M100. The absolute positioning of the final ^{12}CO (1-0) and (2-1) maps, which resulted from a large number of pointing sessions on 3C273, should be better than $\pm 2''$ (r.m.s.).

All the observations were made by switching every 2 seconds the telescope subreflector between the ON position and two comparison fields at $\pm 4'$ in azimuth (using the wobbler switching technique). Particular care was taken to check if the comparison fields were free of CO emission at the studied velocities.

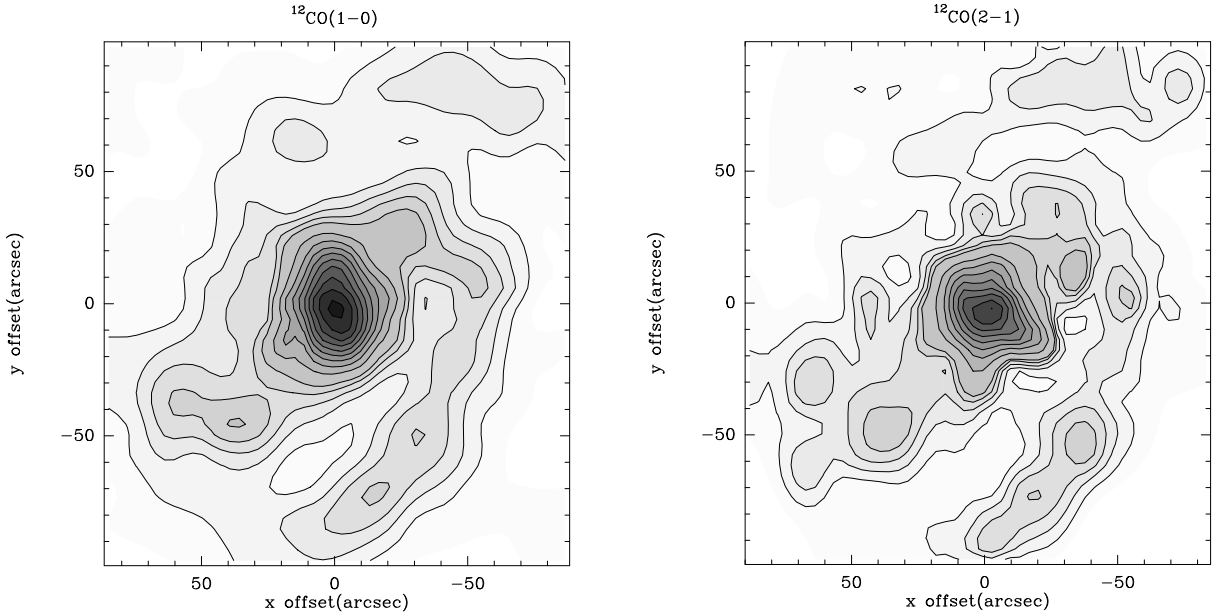

Fig. 1. a (left) The $I_{10}=\int T_a^*(^{12}CO(1\text{-}0))dv$ and **b** (right) $I_{21}=\int T_a^*(^{12}CO(2\text{-}1))dv$ integrated intensity maps in M100. Gray scale and contours are: 4 to 12 by 2 and 17 to 60 by 5 in Kkms^{-1} units, for the 1-0 line, and 2 to 6 by 1 and 10 to 50 by 4 in Kkms^{-1} for the 2-1 line.

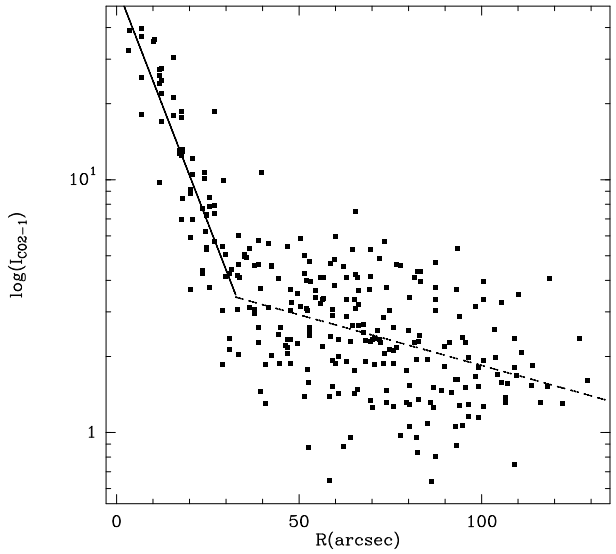

Fig. 2. We represent in logarithmic scale I_{21} against R. Superposed on it are the exponential fits to the disk component (dashed line) and the nuclear disk **ND**(thick line).

The line intensity scale throughout this paper is in units of Ta*, the equivalent antenna temperature, corrected for rear spillover and ohmic losses, reported above the atmosphere. The ^{12}CO (2-1) line integrated intensity, $\int$Ta* dv, will be referred to as I(CO). Ta* is related to T_{MB}, the beam-averaged radiation temperature by Ta*= $\eta_{B_{eff}} T_{MB}$, where $\eta_{B_{eff}}$ is the telescope main-beam efficiency (note that $\eta_{B_{eff}}$ does not include in this definition the forward efficiency η_{forw}). Measurements on Jupiter and Mars yielded $\eta_{B_{eff}}$=0.65 at 115 GHz and 0.46 at 230 GHz.

As an alternative to RA and DEC coordinates we use the x and y axes taken parallel to the major and minor axes, respectively. This allows to include straightforwardly the previous CO data of **GB94** limited to sample the minor axis. Sign conventions define $x > 0$ eastwards, and $y > 0$ northwards, with a position angle PA=150°. The map is centered close to the position of the central radio continuum source ((x, y)=(0,0)= (α(1950)=12^{h}20^{m}23.2^s, δ(1950)=16°06' 00")), very close to the dynamical center determined in this work.

The spatial resolving power of the present observations is of 12″ and 21″, for the 2-1 and 1-0 transitions of ^{12}CO, respectively. The grid of observed positions in ^{12}CO(1-0) and ^{12}CO(2-1) covers a nearly squared region $\Delta X\Delta Y\sim$180″x180″ fully sampled in the 1-0 transition (Δx=Δy=12″). A subset of spectra towards the inner 50″x50″ region of the galaxy have been observed with a 6″ spacing and ∼100 selected positions, spread all over the disk, were observed using the 1-0 line of ^{13}CO .

3. Molecular gas distribution

3.1. The CO maps

Figs. 1a-b show the velocity-integrated 1-0 and 2-1 line intensity contours, respectively. An inspection of Figs. 1a-b unveils roughly the major features defining the distribution of H_2 gas.

– Firstly, CO emission traces distinctly a two-arm highly contrasted spiral pattern. The two arms, notated as I and II, (see Fig. 1a) develop from the ends of a large gaseous bar which is aligned with the stellar bar seen in the optical and infrared

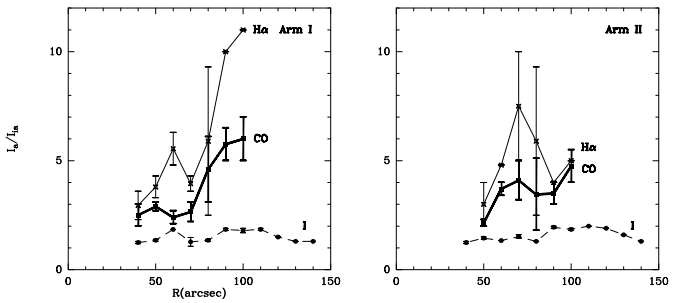

Fig. 3. The arm-interarm contrasts (I_a/I_{ia}) for arms I (left) and II (right) are displayed, as a function of the deprojected radius (R), from CO data (thick line), H_α (thin line) and I band photometric data at 1.65μ. Error bars, centered on the average $I_a/<I_{ia}>$, are indicative of peak to peak values for I_a/I_{ia}.

images of this galaxy. Arm I (II) springs off the western (eastern) side of the bar at a radius of r$\sim$50″. The molecular gas bar has a position angle of PA$\sim$110°, and an apparent major axis diameter of a$\sim$90″($\pm$10″). The two-arm spiral pattern departs markedly from symmetry: if the strength is measured by arm-interarm contrast, arm I is stronger, on average, and it can be followed more continuously than arm II. The latter develops from the bar split up in two armlets, it disappears and finally shows up again at a position angle close to the major axis crossing. The reported splitting is more evident in the higher resolution 2-1 map (Fig. 1b) and it behaves kinematically as a secondary wave compression (see Figs. 7a-b). Moreover, the two arms display different star formation properties and they relate differently to other spiral arm tracers. Different dynamical and kinematical properties underline the asymmetry displayed by the two-arm spiral pattern.

– The CO emission along the bar does not show a flat profile, but it is strongly concentrated towards the nucleus. We can speak of a distinct *nuclear disk component* (**ND**) up to a radius of r_{nucl} $\sim$30″. Although with our spatial resolution we marginally resolve **ND** (even in the 2-1 transition), there is evidence that the latter has a complex substructure to be studied at higher spatial resolution (see paper**II**).
– Although weak, interarm emission is detected nearly everywhere in the observed area. Therefore molecular gas preexist before crossing spiral arms and it is not necessarily created by the density wave. Though there is a good coincidence between the CO arm peaks seen in the 30m map and the narrow lane of bright maxima shown by the Bima interferometer map of Rand (1995), single data show that the CO arms are thick: they have a deconvolved width of 15-18″ (FWHM=1.2-1.5kpc). The corresponding value derived by Rand is slightly lower than ours ($\sim$9-17″), mostly due to the partial flux filtering of low spatial frequencies in his map (a rough estimation gives $\sim$50% of filtering) .
– Typical CO linewidths range on average from 10 to 20 kms^{-1} in the interarm region. Although CO linewidths show different values and radial variations for arms I and II (to be linked with large scale dynamical properties, as discussed in Sect. 5), on average they are larger (20 to 40kms^{-1}) than the equivalent interarm values at the same radius. CO lines become extremely wide towards the nuclear disk (FWHM$\sim$200kms^{-1}) mostly attributable to a steep gradient of the rotation curve within this region and the occurrence of bar+spiral driven non-circular motions.

3.2. The radial distribution

Fig. 2 displays for the 2-1 line (where the resolution is the highest) the radial profile of the measured integrated intesities $I_{CO(2-1)}$ in logarithmic scale . The strong concentration of molecular gas emission towards the nucleus stands out clearly. Besides a nuclear disk extending up to r_{nucl} $\sim$30″, the disk emission decays exponentially from r=30″ to r=150″. The overall radial trend of I cannot be fitted with a single exponential. This is clearly illustrated in Fig. 2 Two distinct components are needed in the fit: one for the nuclear disk with a scale height h_{nucl}=12″($\pm$2″) (fitted with data in the interval Δr=0″-30″) and an additional for the disk characterized by a much larger scale height h_{disk}=87″($\pm$4″) (using data from Δr=30″-100″). The corresponding fitted values for the 1-0 transition are h_{nucl}=15″($\pm$3″) and h_{disk}=67″($\pm$4″). h_{disk} measured in the 2-1 line is significantly larger than the corresponding 1-0 value, which translates into an increasing 2-1/1-0 line ratio radial trend, at least within the interval 30″-100″ (see Sect. 6).

The scatter in the observed I with respect to the fitted exponential law for the disk comes from the mixing of arm, interarm, bar and off-bar points within each radial bin. In particular, points along the major axis of the bar show integrated intensities $\sim$ 2 higher than those along the minor axis for radii r$\sim$30″-50″.

The total molecular gas mass M(H_2) within the sampled region (ΔXxΔY=200″x200″) can be estimated via a standard conversion factor X=N(H_2)/I_{CO}=2.3x10^{20}cm^{-2}K^{-1}km^{-1}s (Strong et al, 1988) applied to the CO luminosity (L_{CO}). We derive M(H_2)=1.2x10^{10}M$_\odot$ if we assume the distance to be D=17.1Mpc. M(H_2) is a factor of $\sim$3 larger than M(H I)=4x10^{9}M$_\odot$ (taken from Knapen et al(1993), and scaled to D=17.1Mpc).

Though M(H_2) might be a lower limit for the total molecular gas content, as we did not sample the whole galaxy disk, the major uncertainties on M(H_2) come from the assumed conversion factor X. There are indications in favour of a lower value X in some *normal* galaxies (M51: García-Burillo et al, 1993; Guélin et al, 1995; NGC891:García-Burillo et al, 1992, Guélin et al, 1993a).

The **ND**, extending up to r$\sim$30″, contains 2.8 10^{9}M$_\odot$, i.e., $\sim$25% of the total H_2 content of the disk. The dynamical mass inside r$\sim$30″ derived from our CO rotation curve is 1.8 10$^{10}M_\odot$. Henceforth, the fraction of molecular gas mass to the total mass content in the **ND** is roughly 16%.

3.3. The arm-interarm CO intensity contrasts

The arm-interarm line intensity ratio is derived from the azimuthal 1-0 distributions in 6 rings of width 10″, obtained by deprojecting and interpolating in the observations grid of Fig. 1. We follow the gas flowing through spiral arms within each radial bin, and consequently the derived arm interarm contrast is not biased by the fall-off of the large-scale emission. We represent in Fig. 3 the arm-interarm ratios for arms I and II, as a function of the galactocentric distance. The arm and interarm intensities (I_a and I_{ia}) are calculated by interpolating in the azimuthal profiles through second-order polynomial fits. Arm-interarm contrasts are defined as $R_{a/ia}$=I_a/$<I_{ia}>$ where $<I_{ia}>$ is the average between the upstream and downstream interarm regions for each arm. Spiral structure is spatially resolved from a radius of r$\sim$30″ and therefore the derived arm-interarm contrast are not affected by beam smearing only from this minimum critical distance outwards.

On average, $R_{a/ia}$ oscillates between 2.5 and 6.5 and it shows an increasing radial trend from r=40″ to r=100″. The maximum contrast is reached in the vicinity of the corotation region (**GB94**, Sempere et al 1995). We must enhance that this result contradicts the abnormally low values given by Cepa et al 1992 and **K96** who claim to find contrasts between 1 and 3. Nevertheless their sampling on the interarm region is poor and they are forced to assume an upper limit detection which overestimate severely I_{ia}. Similar values of $R_{a/ia}$ and also an increasing radial trend towards corotation are observed in the spiral M51 by García-Burillo et al 1993. Numerical simulations have shown that this fits within a scenario where the orbits of preexisting molecular clouds crowd along the spiral arms.

As shown in Fig. 3, $R_{a/ia}$ is systematically higher for arm I than for arm II, except for the interval r$\sim$60-75″ where interarm region for arm II is particularly weak.

Fig. 3 compares the radial variation of $R_{a/ia}$ seen in CO, with their counterparts in H_α and in the I band image. Notwithstanding possible extinction effects, H_α shows the highest values (between 3 and 8, i.e. a factor of 1.5-2 larger than those of CO) contrary to I which shows the lowest (between 1.2 to 2, i.e. a factor of 2 to 3 lower than those of CO). The apparent enhancement of star formation efficiency along spiral arms seems marginal, as $R_{a/ia}(H_\alpha)\sim 2\times R_{a/ia}$(CO). Moreover this result depends on the dubious constancy of the X conversion factor between the interarm and the spiral arm regions (García-Burillo et al (1993) found a X conversion factor 3 times lower for the interarm than for the spiral arms in M51, using radiative transfer models to fit the observed line ratios). In Sect. 6 we also find evidences indicating that $X_{interarm} < X_{arm}$ for M100.

Again, arms I and II behave differently: although, on average, all the tracers show an increasing radial trend, the differences in contrasts between H_α and CO are washed out for r>80″ in arm II.

4. Comparison with other tracers

M100 is a well studied object and analysis of its complex disk morphology using different spiral arm tracers exist already in the literature. We will focus here on the comparison between CO, H I and H_α.

The H I data used are taken from Knapen et al 1993. Here the VLA cube at 20″ resolution, close to the 21″ resolution of our ^{12}CO(1-0) data is used for comparison. We use the new WHT H_α image described by Knapen (1992). To get physically meaning results in the comparison we have degraded the H_α image from its intrinsic resolution of 1″ to 21″ using a gaussian convolution algorithm.

4.1. H_α

Fig. 4a shows an overlay of $I_{CO(1-0)}$ (line contours) with H_α (gray scale) The H_α emission map mimics the strong asymmetry between arms I and II seen in CO: arm II is hardly delineated in Fig. 4a up to r$\sim$ 80″. The bar itself is also a weak H_α emitter except for its end points from which spiral arms stretch out. The strongest emission comes from the nuclear disk and arm I where CO and H_α show an excellent spatial correlation. On the contrary, H_α maxima are displaced $\sim$ 10-20″ outwards relative to the end points of the CO bar. A slight ($\sim$5-10″) H_α-CO offset exists along arm II, where H II regions are downstream (assuming trailing arms).

Such a shift is usually interpreted as being the signature of an evolution sequence driven by the density wave: massive stars visible in H_α (identified at the outer half of the CO arms) are born from GMC assembled from smaller clouds and H I complexes at the entrance of the arms. A scale time between the assumed peak of gas compression and the subsequent MSF episode is naively derived. According to this theoretical scenario, star formation is enhanced and not merely reorganized by the density wave along the spiral arms. However, as shown, we see no "*coherent*" sequence in the disk of M100: the spatial correspondence of H_α and CO clumps is excellent in arm I but it breaks down elsewhere. Correlation along arm I is also discussed by Rand (1995) with interferometer data. Extinction by dust might create at places an artificial anticorrelation between H_α and CO (e.g. as we see in arm II) and therefore deriving time scales from it could be misleading. The high-resolution Bure data show that CO is spatially anticorrelated with H_α, and on the contrary, that CO display a good correlation with thermal radio-continuum (see paper**II**).

Extinction effects can be estimated from ^{13}CO in our map, using the observed correlation between the ^{13}CO velocity-integrated intensity and the visual extinction, A_v derived by Cernicharo and Guélin (1987) for the galactic cloud Heiles 2:

$$I_{1-0}(^{13}\mathrm{CO}) = 1.4(2A_v - 0.7)$$

where I is in Kkms^{-1}, A_v in mag., and the factor of 2 corrects for the dust behind the H II region assumed to be halfway in the disk. This method has been used by García-Burillo et al 1993 to derive A_v in front of H II regions of M51. The authors showed a

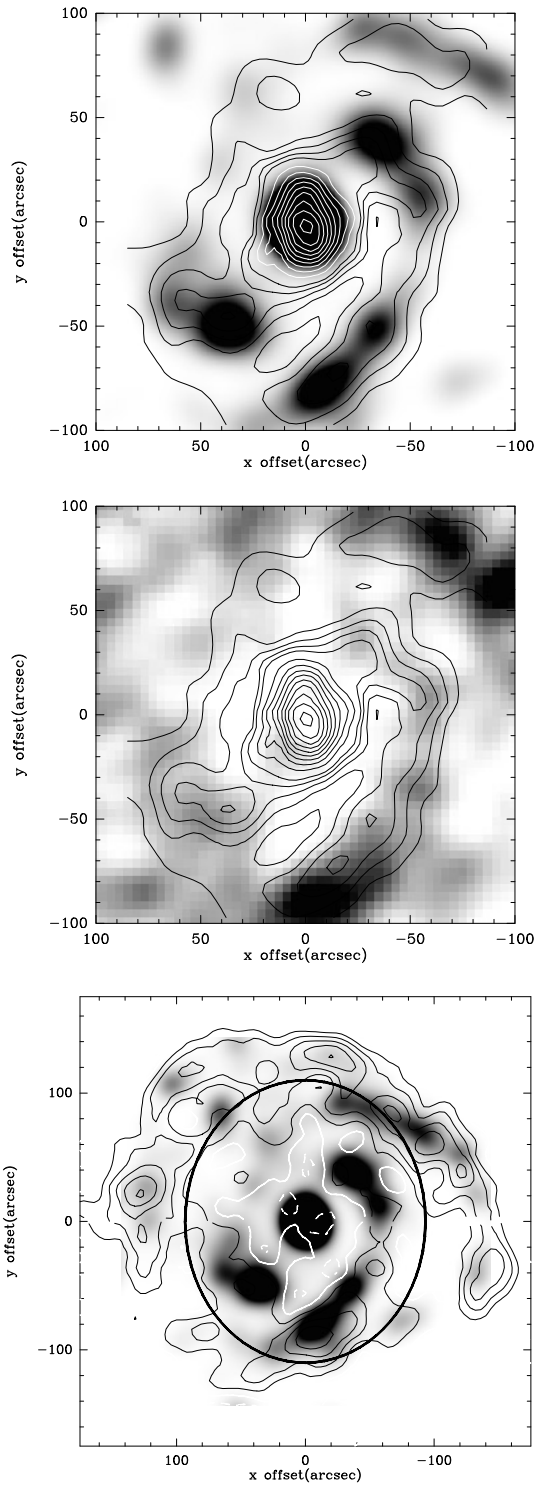

Fig. 4a–c. The I_{10} distribution (with contours identical to Fig. 1a) is superposed to: **a** (top) H_α emission (with gray scale ranging from 0.05 10^6 to 0.3 10^6erg s^{-1}) and **b** (middle) 21cm integrated intensity from H I (with gray scale ranging from 9.42 10^{20} to 22 10^{20} by steps of 3.14 10^{20}atom cm^{-2}). **c** (bottom) Overlay of H I brightness contours and the H_α emission map (gray scale). The ellipse indicates the location of the corotation r_{cor}=110″ according to the fit of Sempere et al (1995).

good correspondence with Balmer decrement estimates of A_v, in spite of the different spatial resolutions of optical (1.5″) and CO data (12″). Henceforth they concluded that A_v is related to gas column density in front of H II regions.

Typical values are A_v=3.5, 1 and 0.4 for the center, arm and interarm regions (the latter values at a radius of r∼60″) respectively. These are lower limits to A_v for two reasons: first, ^{13}CO comes mostly from the dense cloud cores of molecular clouds (tracing unfairly GMC's halos which also contribute to A_v), and secondly, the estimated A_v is only an average within the 21″ 30m lobe (local values in front of H II regions might be larger). Still, the conclusion is that optical extinction effects appear to be significant for the spiral arms and for the nucleus of M100 and, henceforth, "*direct*" comparisons between CO and H_α maps should be taken with caution.

4.2. The Star Formation Rate (SFR)

Further insight to star formation process can be inferred from the radial variation of the ratio $<SFR>=<F(H_\alpha)>/<I_{10}>$ shown in Fig. 5a. We obtain <SFR> from the azimuth-averaged radial profiles $<F(H_\alpha)>$ and $<I_{10}>$. As shown in Fig. 5a, <SFR> shows a strong minimum in the range r=25-50″, coinciding with the bar, delimited by two maxima located towards the nuclear disk and the midpoint where the inner spiral arms develop (r∼70-80″). From this local maximum, <SFR> is almost constant up to the corotation radius (r_{cor}∼100-110″) and it goes down abruptly farther out.

The density wave triggering scenario is unable to explain a maximum in the <SFR> towards corotation, however. In the vicinity of corotation the relative speed between the wave pattern and the gas ($\sim \Omega - \Omega_p$) vanishes, and therefore no classical large scale shock is expected to occur.

The reason behind the abrupt falling of <SFR> from r∼110″ outwards is explained by the development of large-scale gravitational instabilities on neutral gas, set on only from the *critical* gas column density N_c. Below N_c the gas disk is gravitationally stable and star formation would drop sharply (Kennicutt, 1989). N_c can be derived from (Toomre 1964):

$$N_c = \alpha\sigma_v\kappa/3.36G$$

where α is a dimensionless constant near unity, κ is the epicyclic frequency and σ_v is the one dimensional velocity dispersion. We take α=1 (see however Kennicutt, 1989 where an average fitted value of α=0.68 is assumed), κ from **GB94** and assume a constant σ_v=10kms^{-1} (see however Sect. 5). Fig. 5b shows the radial trend of $N(H_2)/N_c$; the points from which $N(H_2)/N_c$ is calculated are taken from the I_{10} map. We distinguish in the adopted typography, the points from the nuclear disk, the arms I-II and the interarm region. Roughly, except from part of the interarm region (where $N(H_2)/N_c$=0.6, on average), the points inside the optical disk lie above the threshold for gravitational instabilities ($N(H_2)>7M_\odot/pc^2$). The ratio $N(H_2)/N_c$ is larger toward the center ($N(H_2)/N_c \sim$ 1.5-3) than along the spiral arms. At close sight we see differences between arm I and arm II. Arm II is marginally above N_c ($N(H_2)/N_c$ ∼0.8-1.1)

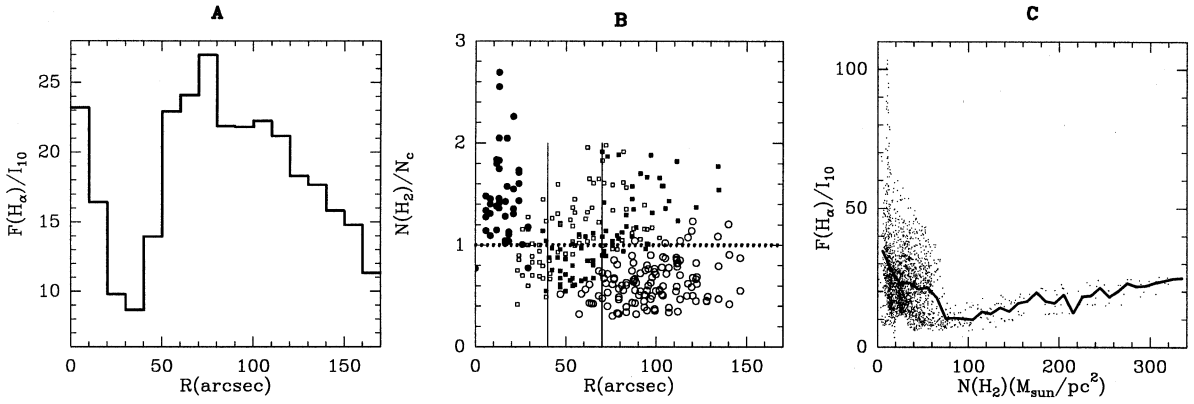

Fig. 5. a Ratio of H_α flux to I_{10} integrated intensities (arbitrary units) as a function of radial distance in M100 disc. **b** Ratio of molecular gas column densities derived from I_{10} ($N(H_2)$) over critical gas column densities (N_c). We distinguish the interarm points as open circles and the ND points as filled circles. Points from arm I (open squares) and arm II (filled squares) are mixed up from r=70" outwards, but they clearly separate in the range r=40-70"(see explanation in the text). **c** Ratio of H_α flux to I_{10} as a function of molecular gas column densities.

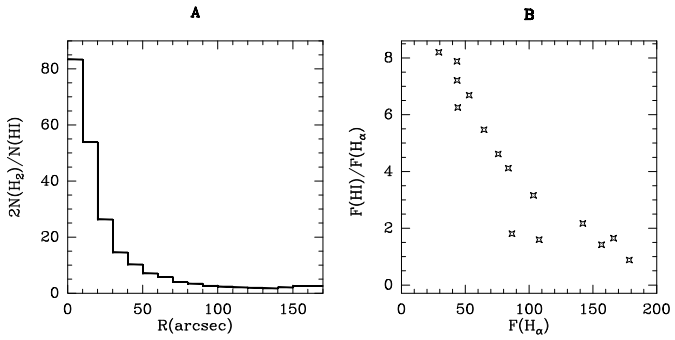

Fig. 6. a Ratio of H_2 to HI column densities against the radial distance. **b** HI to H_α flux (arbitrary units) as a function of H_α flux in M100 disc.

along the segment where it is hardly delineated (the referred interval r=40"-70"), whereas arm II points lie always well above the threshold $N(H_2)/N_c \sim$ 1.2-1.6) for this region. Note that both arms I-II are above the threshold at the outer disk (from r=70" outwards).

The local SFR in the disk (SFR=$F(H_\alpha)/I_{10}$, the 2D version of <SFR>), is represented in Fig. 5c against $N(H_2)$. The thick line represents the average of SFR in bins of $\Delta N(H_2)=10 M_\odot/pc^2$.

SFR is often parametrized as a power law of the neutral column gas density, known as the Schmidt law (Schmidt 1959). The **ND** SFR ($N(H_2)$=100-320$M_\odot/pc^2$) has a mostly linear dependence on $N(H_2)$. Although a detailed analysis of the Schmidt law is beyond the scope of this paper, this result is somewhat surprising, in view of the high $N(H_2)/N_c$ ratio reported above. The large spread of points up to $N(H_2)=100 M_\odot/pc^2$, reflects the mixture of interarm, arms and bar positions. Still, the average SFR on the disk spiral arms is higher than towards **ND**.

One should be aware of the major uncertainties of this kind of analysis: firstly we ignore the bias of extinction on $F(H_\alpha)$, although from this work we suspect H_α to be an unfair tracer of star formation in M100, especially for the **ND** (Sect. 4.1). The linear Schmidt law of **ND** may be an extinction artifact. Note also that the reported H_α ring cannot be resolved with the present resolution. Secondly, the derivation of $N(H_2)$ from I_{10} is made via a dubious X conversion factor which we suspect to be lower than assumed. On the other hand σ_v of **ND** molecular clouds might be $>10 kms^{-1}$, and we might be underestimating N_c for **ND**.

The existence of intense magnetic fields, a high supernova birth-rate and finally the occurrence of strong tidal forces are proposed as possible causes to account for the existence of low star formation rate in the center of our Galaxy. The steepness of the M100 rotation curve indicate that the action of strong tidal forces in the inner 15″ (inside the **ND**) are not to be discarded.

4.3. H I

Fig. 4b overlays $I_{CO(1-0)}$ (line contours) with H I integrated intensity (gray scale). The spatial anticorrelation between molecular and atomic hydrogen stands out in the large scale radial distribution as well as in the spiral structure of the two tracers: H I emission is scarce in the inner disk (up to r∼60″) contrary to CO; H I spiral arms appear always downstream shifted ∼ 5-20″ relative to CO.

Knapen et al (1996) find a tight correlation between H I and H_α complexes, and they invoke the same scenario proposed by Tilanus and Allen (1989, 1991) in M51 to account for it: at large scale, H I might be a photodissociation subproduct (by giant H II regions of OB associations), rather than the source of formation of H_2 clouds. We must note that this spatial correlation is at places very poor, when H I and H_α maps are compared with the same spatial resolution (17″) (see Fig. 4c). Moreover, when we represent the average H I/H_α ratio against the H_α flux in the disk of M100 (Fig. 6b), we clearly see that these magnitudes are perfectly anticorrelated. There is no reason why H II regions cannot photodissociate molecular clouds in the **ND**, where there is hardly any H I flux.

The large scale distribution of H I may be more properly explained by the gravitational instability theory. Similarly to

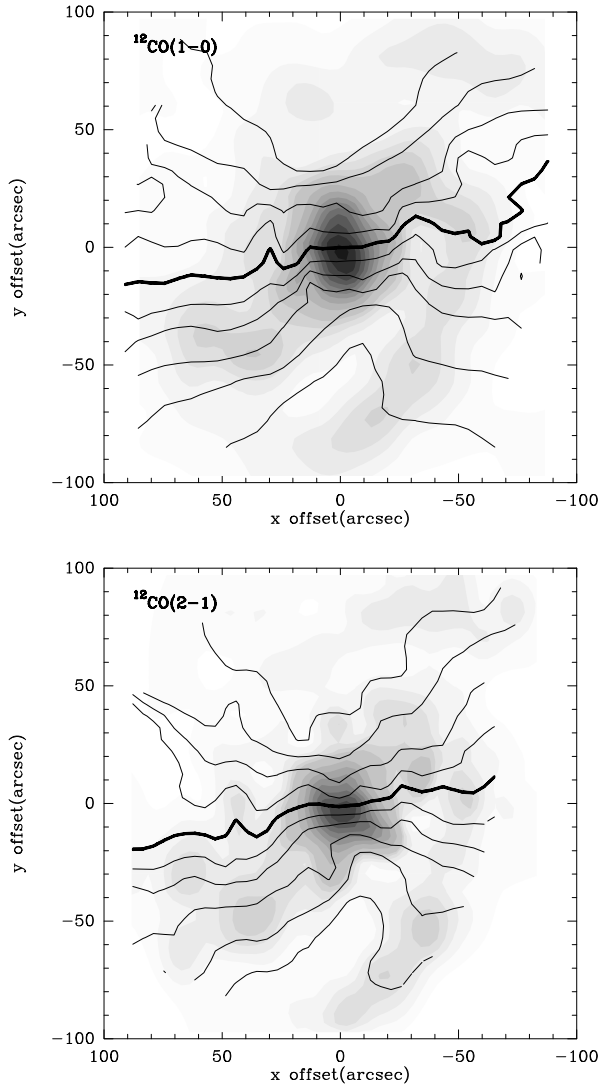

Fig. 7. Overlaid on gray scale images of I_{10} and I_{21} (same levels as in Figs. 1a-b) we plot the first-moment isovelocity contours derived from the 1-0 and 2-1 transitions of ^{12}CO (figures (a)(top) and (b)(bottom), respectively). Isovelocities go from 1450kms^{-1} to 1750kms^{-1} by steps of 25kms^{-1}. Thick contours stand for the systemic velocity v_{sys}=1575kms^{-1}.

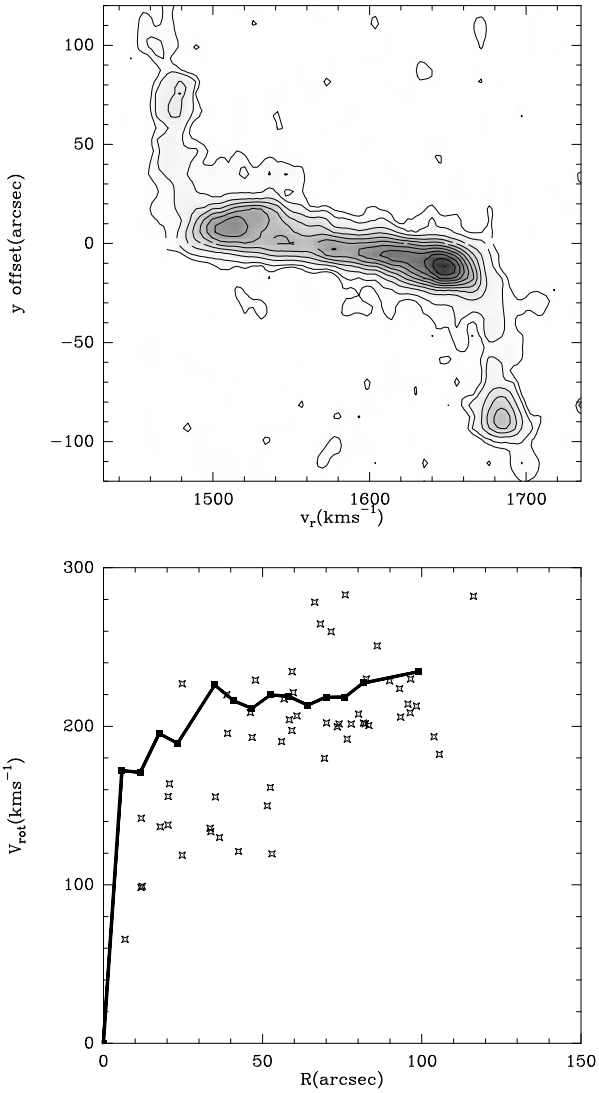

Fig. 8. a The ^{12}CO(2-1) (top) position-velocity diagram taken along the kinematical major axis of M100. Contours and gray scale range from 10% to 90% of the peak values by steps of 10%. **b** Rotation curve (V_{rot}) derived from the terminal velocities of Fig. 8a (thick line) are compared with the values of V_{rot} derived from velocity centroids (see text for explanation).

other galaxies M 100 shows an overabundance of molecular relative to atomic hydrogen in the inner disk up to a certain radius: 2N(H_2)/N(H I) varies from $\sim$ 80 (at r=0 $''$) up to $\sim$ 2 (at r>100$''$) (see Fig. 6a). The phase equilibrium between H I and H_2 holds from a certain radius R_c, where N(H_2) is close to N_c. For r<r_c, H I is mostly converted to H_2 and star formation is set on at large scale. Also, we expect the average pressure to be higher for the **ND** than elsewhere in the disk. This would contribute to shift the equilibrium towards molecular at the expenses of atomic gas as the HI layers are thinner at high pressure than for H_2. A similar scenario has been succesfully invoked to explain the H_2/HI ratio in the nucleus of our Galaxy (Elmegreen and Elmegreen, 1987, see also Elmegreen 1993)).

5. Gas kinematics

Fig. 7a and b shows the velocity field of M 100 obtained from the ^{12}CO(1-0) at 21$''$ resolution (top) and ^{12}CO(2-1) at 12$''$ resolution (bottom), superimposed on the integrated intensity maps. Assuming that the spiral arms are trailing, north corresponds to the approaching side and south to the receding one.

The gas kinematics is mainly dominated by circular rotation but the overall morphology of the velocity field is very distorted due to the complex underlying potential. The velocity maps show deviations from a pure circular rotating pattern. The streaming motions are related to the main bar and the crossing of the spiral arms.

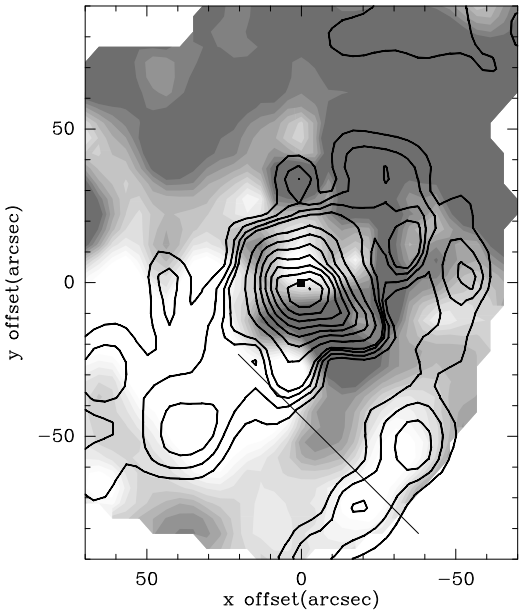

Fig. 9. The ^{12}CO(2-1) residual velocity field showing non-circular motions is represented in gray scale levels equally spaced from -10kms^{-1} to +10kms^{-1} by steps of 2kms^{-1} superposed to the I_{21} map (same contour levels as Fig. 1b starting by 3.). Regions of receding radial velocities appear gray-shaded, while areas with approaching velocities appear white-shaded. The drawn line crossing arm I indicates the location of the strip shown in Fig. 10.

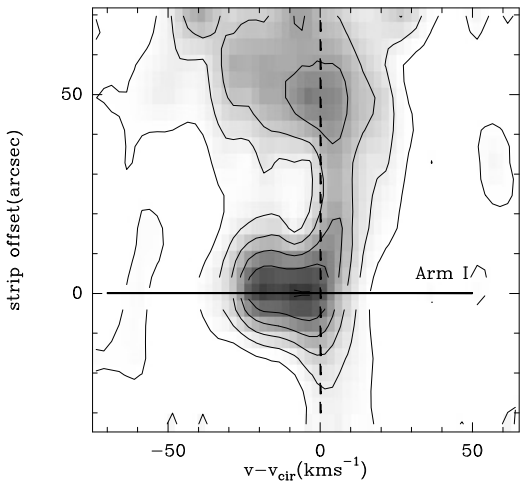

Fig. 10. Position-velocity diagram obtained from the strip taken across arm I (see Fig. 9). Abscissa units are residual non-circular velocities in kms^{-1}. Ordinate units are the arcsecond offsets with respect to the crossing of arm I along the strip.

The *x* and *y* axes defined in Sect. 2 are oriented *a priori* with PA=150°. However the information on the velocity field extracted from CO and H I (for the inner (R<100″) and the outer disk (R>100″), respectively) allows a redetermination of the kinematical major axis and the dynamical center. Using a standard least squares fit algorithm, we find the major axis oriented with PA=153°±1°. The dynamical center position is located at an offset Δx=-3.5″, Δy=-2.5″ close to the dynamical center derived from higher-resolution data (paper **II**) (α= $12^h20^m22.96^s$ δ=16°05′57.5″ (1950)).

Note however that the minor axis is apparently twisted within the region 30″<r<60″, due to bar driven streaming motions. The isovelocity contour v_{sys} = 1575 km s^{-1} tends to align with the major axis of the bar (PA=110°). This is the expected signature on the velocity field of the x_1 family of orbits sustaining the bar. From R∼ ±60″ to the edge of the disk, the kinematical minor axis lies again along PA=153° (see the H I 30″ velocity field of Knapen et al 1993). In the **ND**, isovelocity contours are apparently parallel to the *x* axis.

Though we lack of spatial resolution to study the **ND**, the change of orientation in the apparent minor axis reveal a change in the underlying potential. We defer further discussions of the detailed morphology and kinematics of the molecular gas in **ND** for paper **II**: high-resolution interferometer data unveil a complex substructure consisting of a secondary bar and inner spiral arm structure (see also Sakamoto et al. 1995, and Rand 1995).

5.1. The rotation curve

We have derived the CO rotation curve (V_{rot}) by two methods: **[I]** first, using the terminal velocities derived from the major axis p-v diagram and secondly, **[II]** using the centroids of the 2D velocity field in the disk. In either cases we use the highest resolution provided by the ^{12}CO(2-1) data. Plausibility of **[II]** depends on the degree of beam smearing of the data (the velocity centroid of the gas emission is a poor estimate of V_{rot} if the gradient of large scale motions is not negligible within the beam). Both methods give comparable estimates of V_{rot} for r>30″: from this distance, outwards, the 12″ 30m beam in ^{12}CO(2-1) is sufficient to resolve the velocity field. On the contrary, method **[I]** is mostly suited to estimate V_{rot} in the **ND** where the velocity gradient is remarkably large, as seen in Fig. 8a.

Fig. 8b shows V_{rot}, derived using the ^{12}CO(2-1) major axis p-v diagram of Fig. 8a. Method **[I]** derives terminal velocities, once the contribution of velocity dispersion (∼10km s^{-1}) and velocity channel width (∼5km s^{-1}) have been accounted for (we assume a gaussian velocity distribution in the deconvolution) The most remarkable feature is the steepness of V_{rot} towards the **ND**: V_{rot} reaches 200 kms^{-1} in less than 10″, reflecting the existence of an ultracompact mass component at the nucleus. The steepness of the CO rotation curve is significantly larger to the one derived from H I (Knapen et al 1993) or H_α (Arsenault et al 1988). This is hardly surprising: CO is known to be the best tracer of kinematics in the innermost disk of spirals where H I is deficient or H_α is affected by extinction (Sofue 1996).

The results obtained from interferometric data (see paper **II**) and Sakamoto et al 1995) confirm the accuracy of method **[I]**. At larger distances, CO, H I and H_α rotation curves agree within the errors.

Method **II** computes V_{rot} directly from the velocity centroid at a particular disk position, assuming that only circular motions contribute to the observed radial velocity and taking as parameters for deprojection: i = 32, PA= 153° and v_{sys}=1575kms^{-1}. The points of Fig. 8b correspond to the ensemble of the observed positions in the disk. For the sake of accuracy, we have excluded a region contained within ±20° around the minor axis. The large dispersion displayed by the points reflects the existence of streaming motions on the arm, the interarm and the bar loci. Practically all the points lie below V_{rot} determined by method **I** in the inner region (r<30″) mostly because of beam smearing in the data. Also the presence of the bar distorts the velocity field at least up to r∼60″, inducing streaming motions that are not accounted for in the derivation of V_{rot}. Considering the orientation of the x_1 family of orbits sustaining the bar (PA=110°:i.e., their major axis are near the galaxy minor axis), the disk points used would give an underestimation on V_{rot} as seen in Fig. 8b. A lesser number of points overestimate V_{rot}.

5.2. The streaming motions

A close view of Fig. 7a-b show the different strength and degree of symmetry of the streaming motions in the southern (I) and northern (II) arms. Along arm I, streaming motions can be followed more continuously and their amplitude is stronger than in arm II. The velocity field along arm II reflects again the asymmetry of the gaseous spiral response in M100: a secondary wave compression appears in the eastern side, coinciding with the splitting of arm II. This kinematical feature, present in the 2-1 and the 1-0 maps, assesses our view that we are detecting the signature of the m=3 mode.

Fig. 9 represents the radial velocity residuals map, obtained by subtracting from the radial velocity field the contribution of V_{rot} determined above. The analysis of the velocity residuals map morphology can be used to estimate the position of the corotation resonance. Sempere et al 1995 applied this method, first proposed by Canzian 1993, to the H I velocity field of Knapen et al (1993), but the deficiency of H I in the central region prevented a study of the velocity residuals map in the inner disk. We are now in a position to use CO to test the validity of the corotation estimate. The residual map of M 100 shown in Fig.9 presents one pair of approaching (white)-receding(black) parts symmetrically placed at both sides of the minor axis of the bar and coincident with the strong distortion in the velocity field caused by the bar potential. Moreover, the asymmetry of the bar is obvious: the approaching side(white) is larger than the receding one (black). With the 12″ resolution data, at the nucleus can be seen a split in two new white-black parts, that could be the signature of the nuclear bar detected in the NIR wavelengths. Likewise, the arm-interarm streaming motions are neatly traced and behave as predicted for trailing spiral arms within corotation: two residual velocity segments follow arm I (white) and arm II (black), accompanied by their sign reversed interarm counterparts. This fits within the scenario where both the bar and the molecular spiral pattern lies within their corotation.

If we consider the strip represented in Fig.9, the CO emission appears blueshifted 10km s^{-1} at the interarm region whereas it is redshifted by 20km s^{-1} at the crossing of arm I. The arm-interarm velocity gradient($\Delta V_{NC}/\Delta R$), deprojected onto the plane of the galaxy, is ∼50km s^{-1}kpc^{-1} measured from the interarm to the crest of the arm (the radial velocity changes by 25km s^{-1} in ∼10″. $\Delta V_{NC}/\Delta R$ is ∼2 larger than the one measured in the interferometer map of Rand (1995). This would seem somewhat paradoxical, considering that our spatial resolution is twice lower than his(12″ compared to 5 ″). However we do include in $\Delta V_{NC}/\Delta R$ the contribution to the streaming of the interarm gas that Rand failed to detect and that might rise the measured slope. In the position-velocity diagram along the minor-axis (see **GB94** Fig. 3) $\Delta V_{NC}/\Delta R$ is similarly ∼30km s^{-1} kpc^{-1}.

An inspection of Fig. 10, representing the p-v plot of the strip of Fig. 9, suggests that we still might be underestimating $\Delta V_{NC}/\Delta R$: the CO velocity profile at the crossing of the arm shows two peaks. Our spatial resolution seems unsufficient to resolve completely the observed velocity jump and properly measure $\Delta V_{NC}/\Delta R$. This enlargement might be due to unresolved streaming motions within the beam. There is a remarkable similarity between this diagram and the one published in García-Burillo et al (1993a), for M 51 (see Figs. 16a-b). Molecular clouds enter the arm from the interarm region in a direction nearly perpendicular to the arm (depending on the spiral arm strength), and their orbits orientation change abruptly as they tend to *stay longer* along the spiral arm potential. Ballistic simulations of the clouds hydrodynamics in spiral disks show that orbits can change abruptly their orientation at the crossing of spiral arms (Combes and Gerin 1985; García-Burillo et al 1993b; Sempere et al 1995). The two peaks seen in Fig. 10 at the location of arm I, could correspond to the two cloud populations (entering and coming out of the arm) having two distinct radial velocity projections. Only the combination of interferometer and single-dish observations (with both the resolution and sensitivity requirements) can clarify this point.

CO linewidths are systematically higher for the arms (FWHM=25-40kms^{-1}) than for the interarm region (FWHM=10-20kms^{-1}). This result holds for CO spectra taken at the same galactocentric radius with a similar contribution from the rotation curve gradient within the beam. The apparent velocity dispersion (σ_v) of molecular gas in the interarm region is of 5-7kms^{-1}, being twice higher for spiral arms. As stated above, we suspect unresolved streaming motions to be partially responsible of the enlargement of CO lines, especially form Arm I (FWHM=30-40kms^{-1}), where streaming are the largest and where some spectra display two peaks: this might reflect the sampling of two cloud populations. However large linewidths on arm I are not always related to two-peaked profiles, but to gaussian-like lines. The energy input from massive star formation on the arms might contribute to enhance the internal cloud velocity dispersion. On the other hand, a higher cloud collision rate along the arms, can rise the cloud-cloud velocity dispersion (García-Burillo et al (1993b), Sempere et al 1995). Arm II shows narrow lines (FWHM∼20kms^{-1}) in the region where

it is split: excepted their higher peak intensity, on-arm spectra are indistinguishable from their interarm neighbors. However near the major axis crossing, where arm II *reappears*, CO lines become wider (FWHM=30-40kms^{-1}). Along arm II, the set on of massive star formation is accompanied by an enlargement of the CO spectra.

6. The line ratios

We observed simultaneously the 2-1 and 1-0 lines of ^{12}CO over the region shown in Figs. 1a-b and the 1-0 isotopic line of ^{13}CO (towards selected areas) to study the possible variations of physical conditions of molecular gas in M100.

We have obtained the radial variation of the 2-1/1-0 line ratio of ^{12}CO (noted as $R_{2-1/1-0}$=$\int T_{mb}^{2-1}dv/\int T_{mb}^{1-0}dv$) from the azimuthal averages of the 2-1 and 1-0 maps, once the 2-1 map was degraded to the resolution of the 1-0 to get the physical parameters of the gas in the same region. On average, $R_{2-1/1-0}$ is higher in the nuclear disk source than in the disk: $<R_{2-1/1-0}>$(**ND**)$\sim$0.8 and it reaches $\sim$0.9 at the center, contrary to $<R_{2-1/1-0}>\sim$0.6 for the disk. Besides, $R_{2-1/1-0}$ increases monotonically from $R_{2-1/1-0}$=0.5 (at r=30$''$) up to $R_{2-1/1-0}$=0.7 (at r=100$''$). We have studied also the variation of the 2D version of $R_{2-1/1-0}$ depending on the particular environment in the disk. At a given radius, $R_{2-1/1-0}$ is significantly lower in the interarm region($\sim$0.5$\pm$0.05) than in the spiral arms region ($\sim$0.65$\pm$0.05).

We have derived the radial variation of the isotopic ratio ^{12}CO/^{13}CO for the 1-0 line (noted as $R_{12/13}$). $R_{12/13}\sim 11\pm1$ for the nuclear disk, significantly larger than the disk value $R_{12/13}\sim 7\pm1$. Contrary to $R_{2-1/1-0}$, $R_{12/13}$ shows no radial trend in the disk. We also analyzed the 2D variation of $R_{12/13}$, depending on the particular location in the disk. We have integrated $\sim$ 1-2 hours on two positions in the interarm region and mapped the spiral arms at different radii. The results indicate a higher $R_{12/13}$ in the interarm ($\sim$15$\pm$2) than in the spiral arms ($\sim$7$\pm$1).

The two independent line ratios ($R_{2-1/1-0}$ and $R_{12/13}$) were analyzed to derive the molecular clouds characteristics using the Large-Velocity-Gradient transfer code. We used a one component model (i.e. we fit using an *average* molecular cloud) to account for the observations. The parameter x(CO)$/(dv/dr)$ was varied between 10^{-5}pc.km^{-1}s and 10^{-4}pc.km^{-1}s (this variation range determines the variation of the model fitted physical parameters) and assumed an isotopic abundance ratio of ^{12}CO/^{13}CO=50, intermediate between the Galactic Center value (25, e.g. Guesten et al 1985) and the ratio holding for the solar neighborhood (75, e.g. Wilson et al 1981). From standard density(n_{H_2})-kinetic temperature(T_K) LVG diagrams (see e.g., Figs. 9a-c of García-Burillo et al 1993) we derive different physical parameters for the *average* molecular cloud in the center, the spiral arms and the interarm region. The best fit for the interarm region shows that CO emission comes from diffuse ($n_{H_2}\sim$150-450 mol cm^{-3}) and cold ($T_K\sim$10-20K) molecular gas. On the contrary, the solution adopted for the center and the arms imposes a higher density medium in either cases ($n_{H_2}\sim$350-2000 mol cm^{-3}; the center and the arms are nearly indistinguishable in the average densities). Note that within the range of the varied parameters (basically x(CO)$/(dv/dr)$), the density is at least a factor of 2-4 higher in the center+spiral arms than found in the interarm region. The best fitted value of the temperature for the arms ($T_K\sim$10-20K) seems to be no significantly different from the interarm solution. Only the **ND** gas seems to be silghtly hotter than the disk gas: $T_K\sim$20-60K.

We would need other line transitions involving other molecular species to complete a self consistent model of molecular gas. García-Burillo et al (1993) presented a radiative transfer based model (LVG and Montecarlo) to account for the line ratios and intensities observed in M51 for the 1-0, 2-1, 3-2 lines of ^{12}CO, the 1-0 and 2-1 lines of ^{13}CO and the 1-0 line of HCN. Their main conclusion is that the conversion factor between N(H_2) and I(CO) is $\sim$ 3 times lower than the Strong's reported value (X=N(H_2)/I_{CO}=2.3x10^{20}cm^{-2}K^{-1}km^{-1}s; see Strong et al 1988). Moreover they derived a 5 times lower conversion factor for the interarm gas. The latter conclusion depended mostly on the average density for interarm model clouds being 3-4 lower than the spiral arms clouds. Recently, Guélin and collaborators found also a lower conversion factor modeling the mm-continuum emission from dust in N891 (Guélin et al 1993) and in M51 (Guélin et al 1995). As stated above, we lack of other transitions to calibrate *absolutely* the M100 X-conversion factor and bolometer observations are still in progress. However, the adopted solution in M100 suggests also that the X factor for the interarm gas is 3-4 times lower than the value adopted for the center+arms gas. As a result of it, the arm-interarm column density contrast would be a factor of 3-4 larger than the arm-interarm I(CO) contrast reaching similar values than indicated by H_α. In view of these figures, there would be hardly any evidence of a significantly higher star formation efficiency along the spiral arms of M100.

7. Discussion

The optical morphology of *grand-design* spiral galaxies are characterized by the presence of mostly symmetric spiral arms. Frequently, the symmetric m=2 spiral mode is accompanied by another symmetric m=2 mode, in the shape of a bar. However optical appearance of spirals, dominated by population I objects, can be misleading: there can be higher (or lower) order modes hidden in the disks, whose lower weight relative to the main m=2 mode make them more difficult to detect by traditional methods. **E92** have published an optical survey of 18 spiral galaxies and discussed a method based on computer-enhancement of photometric plates to emphasize the occurrence of m=3 modes in disks. The majority of the galaxies studied (among them, NGC4321) showed the development of three symmetric arms between the inner and outer 3::1 resonances (they implicitly assumed a common pattern speed for the m=2 and m=3 mode). The point of the theory suggests that the three spiral arm pattern is the result of the interplay between the m=2 symmetric spiral mode and a non negligible asymmetric m=1 component. Occurrence of m=1 modes instabilities is likely in spiral disks (Junqueira and Combes, 1996).

In the case of M100, and adopting the pattern speed derived by **GB94** (Ω_p=20kms^{-1}kpc^{-1}), the inner and outer 3::1 resonances should lie at r$\sim$40-50$''$ and r$\sim$190$''$. The antisymmetric enhanced images of the galaxy show with little doubt the development of a three spiral mode within the specified interval. The existence of secondary modes in spiral disks should be properly corroborated by using gaseous tracers which respond strongly to density wave forcing as a result of their lower velocity dispersion, compared to the stars.

In the previous sections we have underlined that a noticeable asymmetry shows up both in the morphology and in the kinematics displayed by molecular gas in the disk of M100: the two spiral arms (which differ in strength and in pitch angle) stretch out from a slightly off-centered bar. Still, the weakest arm II is split in two arms-lets which show up kinematically as a secondary wave compression and it appears again at r$\sim$80$''$. The splitting (more evident in the integrated intensity and isovelocity ^{12}CO(2-1) map) starts at r$\sim$40-50$''$, i.e., near the locus of the inner 3::1 resonance according to **E92**. Moreover, one of the anomalous arm-lets follows one of the optically identified three arms (see plate 10 of **E92**). The same asymmetry can be identified in the two spiral arm potential by looking at the K-band image of Sakamoto et al 1995. Arm II changes its pitch angle and stretch out from the bar at a different radius than arm I. Still, the distortions and kinks are to be linked with the optically detected three arm structure. The response of gas to this asymmetric spiral potential is indeed asymmetric: Sempere et al, 1995 hydrodynamical simulations of the molecular gas response reproduces fairly the splitting on the northern arm as well as the off-centering of the bar. The potential derived from the infrared image used in this work contained already the reported asymmetries.

Moreover CO is not the only gaseous tracer which shows evidences of an asymmetrical response in the inner disk (inside $\sim$10kpc). As discussed in Sect. 4, star formation traced by H_α is significantly larger for arm I compared to arm II within the interval 50$''$ <r<100$''$; star formation reappears in arm II only outside corotation (r$\sim$110$''$).

We must enhance that so far there is no clear understanding of what would be the response of the neutral gas component to a packet of coexistent different wave modes. The response of the gas, even in the simplest case of a well defined quasistationary spiral may be time dependent (Roberts and Stewart, 1987): molecular gas presents a clumpy *fractal* structure and how it responds to a spiral density wave depends on several factors which vary from galaxy to galaxy (magnitude of the mean free path in cloud-cloud collisions, strength of the spiral potential, existence of several modes in the disk at interplay, etc.). Numerical simulations have shown that molecular arms may slosh back and forth the spiral potential well minimum, as a function of time and radius. The ensemble of molecular clouds cannot reach a steady state even after several rotation periods (Casoli and Combes, 1982; Combes and Gerin 1985).

Henceforth, in the case of M100, where there are evidences suggesting the presence of a m=3 mode superposed to the spiral+bar, the classical scenario to interpret the sequence of star formation tracers in spiral arms is bound to fail, as discussed in Sect. 4.

There are several observational evidences indicating that M 100 is an *evolved* grand design spiral:

- The infrared imaging of the nucleus has shown the presence of a small oval within the inner 15$''$. The existence of nested bars is interpreted as a sign of evolution: bars are powerful engines which propitiate the gas inflow to the center of galaxies (the **ND** of M100 has a strong concentration of molecular gas). Gas material is gradually accumulated in the nuclei and subsequent star formation increases the mass of bulges. As gas material is progressively swept inwards, a second nuclear bar instability develops. Therefore, bars are viewed as fueling engines of secular evolution inside the Hubble sequence.
- The inhibition of SF along the M100 bar is also a signature of evolution. In contrast with *young* bars, *evolved* bars have a low star formation activity, as shown by the numerical simulations of Friedli and Benz (1995). After a starburst phase, the energy injection from supernovae inhibit subsequent star formation episodes along the bar.
- Elmegreen et al (1989) identified the resonance responses at the OLR, the corotation and the 4::1 resonances in the optical pictures of M100. A strong response at resonances located in the outer disk can appear only in evolved disks (as numerical simulations seem to indicate).
- The CO distribution and kinematics of M 100 suggests the existence of a three-arm structure. **E92** have interpreted the existence of m=3 spiral structure in terms of galactic evolution: an initially symmetric m=2 mode (set on by the passing of a close companion) can become asymmetric and eventually induce a m=1 mode which couples with the m=2 mode to drive a m=3 spiral. The three-arm spirals would be driven waves (not independent waves modes) and a likely source of energy loss from the two-arm mode.

Contrary to M51, which is a markedly interacting system with a strong m=2 spiral, M100 is apparently isolated (there are no nearby candidates of companion galaxies). At least, a close passage of a companion has not occurred in the immediate past. The spiral wave strength for M51 (measured by the $R_{a/ia}$ contrast and the streaming motions) is higher than in M100. Though the m=2 mode is still predominant in M100, other secondary modes seem at interplay reflecting the secular evolution of the disk.

8. Summary

We summarize the main results of this work as follows:

- CO emission is detected in M 100 disk up to r$\sim$12kpc and shows a contrasted two-arm spiral pattern that develops from a molecular bar. The spiral pattern is markedly asymmetric. The asymmetry is reproduced in the H_α and the NIR wavelengths. Arm II stretching out from the eastern side of the bar is split up from r$\sim$50$''$ up to the major axis crossing on the northern side. This feature is identified as the signature

of the gas response to the m=3 mode detected by **E92** in enhanced optical I-band images of M 100.

– CO emission is strongly concentrated toward the nucleus. A *nuclear disk component* is distinguishable from the main bar within a radius $r_{nuc}\sim30''$. The fraction of molecular gas mass to the total mass in the **ND** is $\sim$16%. The high concentration of molecular gas in the **ND** could be the signature of gas inflow toward the center.
– The arm-interarm contrasts, $R_{a/ia}$, oscillate between 2.5 and 6.5 and show an increasing radial trend from r=40″ to r=100″. On average, $R_{a/ia}$ is systematically higher for arm I than for arm II. The maximum contrast is reached at the boundaries of the CR. $R_{a/ia}(H_\alpha)$ is a factor 1.5-2 higher than the $R_{a/ia}$(CO). The Star Formation Efficiency (measured by $F(H_\alpha/I_{CO})$ is marginally enhanced along spiral arms: the $X=N_{H_2}/I_{CO}$ conversion factor is suspected to be overestimated in the disk, especially for the interarm region.
– The SFR shows a minimum in the range r$\sim$20-50″, coinciding with the bar, delimited by two maxima located in the **ND** and in the region where the spiral arms stretch out from the edges of the bar. The SFR is almost constant up to the corotation radius r_{cor} $\sim$100-110″ and goes down abruptly farther out. Contrary to what is expected by the density wave triggering scenario, the comparison between CO, H I, and H_α maps shows that there is no *coherent* sequence in the relative location of the star formation tracers along the spiral arms. Extinction effects could be significant and might create artificially CO-H_α offsets.
– The CO rotation curve is steeper than shown by H I and H_α: it reaches 200km s^{-1} within the inner 1kpc, reflecting the high mass concentration of the **ND**. The velocity field shows the streaming motions related to the spiral+bar wave. The asymmetry seen in the molecular spiral structure is mimicked by the gas kinematics: streaming motions in arm I are of higher amplitude than in arm II. A second wave compression at r$\sim$30″ in arm II traces the m=3 mode present in the stellar potential.
– The line ratios $R_{2-1/1-0}$, $R_{12/13}$ were analyzed to derive the molecular cloud physical parameters using a one component LVG model. The interarm region shows that CO emission comes from diffuse ($n_{H_2}\sim$150-450mol cm^{-3}) and cold ($T_K\sim$10-20K) molecular gas. The gas density found in the center and the arm regions is 2-4 higher than found in the interarm region and only the **ND** gas seems to be slightly hotter than the disk gas ($T_K\sim$20-60K). Even if we need more observations in other line transitions to complete a model of the molecular gas, this result suggests that the X factor for the interarm gas could be 3-4 times lower than for the center and the spiral arms.

Acknowledgements. We thank F.Combes for useful discussions and comments on the manuscript. We also thank J.Knapen for providing us with the H I and H_α data cube used in this paper. This work has been partially supported by the Spanish CICYT under grant number PB93-0408.

References

Canzian B., 1993, ApJ, 414, 487
Casoli F., Combes F., 1982, A&A, 110, 287
Cepa J., Beckman J.E., Knapen J.H., et al., 1992, AJ, 103, 429
Cernicharo J., Guélin M., 1987, A&A, 176, 299
Combes F., Gerin M., 1985, A&A, 150, 327
Elmegreen B.G., Elmegreen D.M., 1986, ApJ, 311, 554
Elmegreen B.G., Elmegreen D.M., 1987, ApJ, 320, 182
Elmegreen B.G., Elmegreen D.M., Seiden P.E. ,1989, ApJ, 343, 602
Elmegreen B.G., Elmegreen D.M., Montenegro L., 1992, ApJS, 79, 37. **E92**
Elmegreen B.G., 1993, ApJ, 411, 170
Elmegreen B.G., 1994. In: King I. (ed). The Gaseous and Stellar Disks of the Galaxy. Astronomical Society of the Pacific Conference Series.
Friedli D., Benz W., 1995, A&A, 301, 649
García-Burillo S., Sempere M.J., Combes F., 1994, A&A, 287, 419. **GB94**
García-Burillo S., Guélin M., Cernicharo J., 1993a, A&A, 274, 123
García-Burillo S., Combes F., Gerin M., 1993b, A&A, 274, 148
García-Burillo S., Guélin M., Cernicharo J., 1992, A&A, 266, 21
Guélin M., Zylka R. Mezger P.G., et al., 1995, 298 29
Guélin M., Zylka R. Mezger P.G., et al., 1993, A&A, 279, 37
Guesten R., Henkel C., Batrla W., 1985, A&A, 149, 195
Junqueira S., Combes F., 1996, A&A, 312, 703
Kennicutt R.C., 1989, ApJ, 344, 685
Knapen J.H., 1992, Ph. D. thesis, Univ. de La Laguna
Knapen J.H., Cepa J., Beckman J.E., et al., 1993, ApJ, 416, 563
Knapen J.H., Beckman J.E., 1996, MNRAS, 283,251
Knapen J.H., Beckman J.E., Cepa, J., Nakai N., 1996, A&A, 308, 27. **K96**
Pierce J.P., 1986, AJ, 92, 285
Rand R.J., 1995, AJ, 109, 2444
Rauscher B.J., 1995, AJ, 109, 1608
Roberts W.W., Stewart G.R., 1987, ApJ, 314, 10
Schmidt M., 1959, ApJ, 129, 243
Shaw M., Axon D., Probst R., Gatley I., 1995, MNRAS, 274, 369
Sempere M.J., García-Burillo S., Combes F., Knapen J.H., 1995, A&A, 296, 45
Sakamoto K., Okumura S., Minezaki T., et al., 1995, AJ, 110, 2075
Sofue Y., 1996, ApJ, 458, 120
Strong A.W., Bloemen J.B.G.M., Dame T.M., et al., 1988, A&A, 207, 1
Tilanus R.P.J., Allen R.J., 1989, ApJ, 339, 57
Tilanus R.P.J., Allen R.J., 1991, A&A, 244,8
Toomre A., 1964, ApJ, 139, 1217
Vaucouleurs G. de, Vaucouleurs A. de, Corwin H.G., et al., 1991, Third Reference Catalogue of Bright Galaxies. Springer Verlag, New York.
Wilson R.W., Langer W.D., Goldsmith P.F., 1981, ApJ, 243, L47

This article was processed by the author using Springer-Verlag LaTeX A&A style file *L-AA* version 3.